JGR Space Physics

RESEARCH ARTICLE
10.1029/2020JA028378

Horizontal Internal Gravity Waves in the Mars Upper Atmosphere From MAVEN ACC and NGIMS Measurements

Yawen Li[1], Jiandong Liu[1], and Shuanggen Jin[1,2]

[1]School of Remote Sensing and Geomatics Engineering, Nanjing University of Information Science and Technology, Nanjing, China, [2]Key Laboratory of Planetary Science, Shanghai Astronomical Observatory, Chinese Academy of Sciences, Shanghai, China

Key Points:

- Horizontal internal gravity waves (hIGWs) in the Mars atmosphere are obtained and illustrated from Mars Atmosphere and Volatile EvolutioN accelerometer and Neutral Gas and Ion Mass Spectrometer measurements
- Interannual variabilities of hIGWs are investigated with linking both dust storms and topography
- Coupling processes between hIGWs and dust storms are presented

Correspondence to:
J. Liu and S. Jin
jd_liu@nuist.edu.cn;
sgjin@nuist.edu.cn,
sg.jin@yahoo.com

Citation:
Li, Y., Liu, J., & Jin, S. (2021). Horizontal internal gravity waves in the Mars upper atmosphere from MAVEN ACC and NGIMS measurements. *Journal of Geophysical Research: Space Physics*, *126*, e2020JA028378. https://doi.org/10.1029/2020JA028378

Received 19 JUN 2020
Accepted 12 NOV 2020

Abstract Internal gravity waves (IGWs) play an important role in the planetary atmospheres, which transfer energy and momentum from the lower layers to the upper atmosphere. However, the IGW perturbations and behaviors are not clear in the Mars upper atmosphere, particularly for the horizontal internal gravity waves (hIGWs). In this study, the hIGWs in the upper atmosphere of Mars are estimated and investigated for the first time using both accelerometer (ACC)-derived mass density and Neutral Gas and Ion Mass Spectrometer-measured neutral density from Mars Atmosphere and Volatile EvolutioN (MAVEN) mission. The results show that the amplitudes of hIGWs variations are significantly affected by the dust storms and increase with the altitudes. The larger amplitudes are triggered in Martian Year (MY) 34 during a global dust event. The characteristics of Ar and CO_2 hIGWs variations are similar. Furthermore, the trend of the CO perturbations seems to follow the CO_2. However, the dust storms play little role in shaping hIGWs of atomic O. The hIGWs show the stable waveform with the increasing altitudes.

1. Introduction

Mars thermosphere is a transition region from the well-mixed lower atmosphere to higher atmosphere where gases become thinner and lost to the space (Deighan et al., 2015; Zurek et al., 2015). The internal gravity waves (IGWs) have great importance on the energy transfer and momentum budget of the planetary atmospheres (Medvedev & Yiğit, 2012; Yiğit & Medvedev, 2015). The structures caused by vertical or horizontal variations are interpreted as vertical or horizontal internal gravity waves (hIGWs). IGWs have a fundamental effect on the dynamics/thermal of planetary atmospheres by redistributing momentum and energy by propagating through layers (Yiğit et al., 2015). Recently, several Mars missions were launched (Albee et al., 1998; Jakosky et al., 2015; Tolson et al., 2005; Zurek & Smrekar, 2007), which provided good opportunities to estimate the detailed IGWs variations.

The IGWs have been observed in the atmospheres of Mars, including thermosphere (Fritts et al., 2006; Müller-Wodarg et al., 2006; Terada et al., 2017) by former missions. Medvedev and Yiğit (2012) and Siddle et al. (2019) showed that the thermal effect of these IGWs is a key physical mechanism in the Mesosphere and low thermosphere (MLT), which is not included in the contemporary Martian GCMs. The amplitudes of IGWs inferred from descent profiles, Mars Global Surveyor (MGS) radio occultation, and accelerometer data have apparent variations at higher altitudes, suggesting that IGWs play a very important role in the upper Martian atmospheric dynamics as well (Fritts et al., 2006). Therefore, the observations and studies of IGWs behavior and characteristics are important in understanding the processes that control the current Martian thermospheric circulation. Nevertheless, the response of thermospheric hIGWs to the surface dust storm is a vital point that could have influences on that processes.

In the past, the vertical component of IGWs have been observed, especially from the Neutral Gas and Ion Mass Spectrometer (NGIMS) onboard the MAVEN mission (Siddle et al., 2019; Terada et al., 2017; Yiğit & Medvedev, 2015). Terada et al. (2017) have reported that the amplitude of vertical IGWs perturbations in the Martian thermosphere was highly related to the background temperatures, meaning that the convective instability causes saturation in the Martian upper thermosphere. Perturbations extracted from NGIMS data in December 2014 between 180 and 220 km demonstrated that IGWs could propagate from lower atmosphere

to thermosphere directly, which showed the significance of both dynamical and thermal IGW effects (Medvedev & Yiğit, 2012; Yiğit et al., 2015). Siddle et al. (2019) and Müller-Wodarg et al. (2006) showed that the perturbations as gravity waves extracted by the temperature and density profiles have vertical wavelengths of around 10–30 km and amplitudes of around 10%. The IGWs in the upper thermosphere with long vertical wavelength are assumed to be the sources of the waves seen in Ar, CO_2, and N_2 from NGIMS observations (England et al., 2016b), which suggests that gravity waves play a significant part in the heating and cooling in Martian atmosphere. Additionally, more studies about gravity wave activities, and the vertical distributions from 120 to 260 km based on NGIMS data were reported by Bougher et al. (2015a) and Bougher et al. (2017). In contrast, there are not many studies on horizontal component of IGWs. Creasey et al. (2006) observed small-scale density perturbations from MGS-derived ACC data and interpreted the structures in the thermosphere to be horizontal with wavelengths of 100–300 km. Fritts et al. (2006) used the similar method based on ODY-derived ACC data to obtain hIGWs as well and found that the amplitude vary significantly with season. However, the characteristics of hIGWs in the Martian thermosphere are not clear, especially the behaviors during dust seasons. The relationship between hIGWs and dust storms could help us understand the response of hIGWs at different altitudes to dust storms and the accuracy of IGW parameterization in general circulation models.

In this study , the hIGWs are estimated from MAVEN ACC-derived densities and NGIMS observations at a long range of vertical altitudes through three different Martian Years (MYs). The seasonal changes of hIGWs and the relationship with the dust storm activities are investigated in detail. The paper is organized as follows. Section 2 describes the data from MAVEN ACC and the NGIMS and the methods of hIGWs estimation. The amplitudes of hIGWs variations and their temporal-spatial variability are analyzed and presented in Section 3. Section 4 shows the mechanism and discussion. Finally, conclusions are given in Section 5.

2. Data and Methods

2.1. Accelerometer and NGIMS Data

During the early aerobraking phase of Mars Global Surveyor (MGS), Mars Odyssey (ODY), and Mars Reconnaissance Orbiter (MRO), onboard accelerometers were mainly used to detect the upper atmosphere structure in term of in situ measurements (Keating et al., 1998; Tolson et al., 2007; Wilson, 2002; Withers & Paul, 2006). Similarly, the accelerometer on board MAVEN can sense atmospheric drag during the aerobraking processes. More details can be found in Zurek et al. (2015). Here, the accelerometers on MAVEN are used to estimate atmospheric density, which requires sufficient signals to make sure that these perturbations are much above the noise level of the instrument and have enough coverage at certain altitude. The accuracy of the measurement can be seen in Liu et al. (2019). The altitudes of 160–170 km have both good global coverage and appropriate accuracy. Although the accuracy of 180 km is not high, the data are stable in autumn and winter. The accuracy is better than that in spring and summer as well. Therefore, we will only estimate the density observations in these altitudes. All of the observations are available publicly on the NASA Planetary Data System (PDS) (https://atmos.nmsu.edu/PDS/data/PDS4/MAVEN/). Figure 1 shows the coverage of ACC data in different seasons used in this study . The periapsis occasionally goes down to ~120 km during "deep dip" campaigns (Zurek et al., 2015). Due to the change of instrument operating mode (Terada et al., 2017), data obtained before February 11, 2015 are not included in this study although they are available in the website, which is consistent with the data range of NGIMS used here.

The NGIMS instrument on MAVEN is a quadrupole mass spectrometer, which can be used to measure atmospheric densities at altitudes below 500 km above the areoid by using a combination of closed and open source channels. Nonreactive species (e.g., CO_2, Ar, N_2, and He) are only observed in closed source channel, however, reactive and nonreactive species can be measured in the open source channel (e.g., CO, NO, O, and ions). Four main neutral densities of species Ar, CO_2, CO, and O are used in this study.

However, we have noticed a fact that CO and N_2 have the same mass of 28 amu for their most abundant isotopes (England et al., 2016b). In order to distinguish them, some known fraction of N_2 breaks up into N inside the instrument to infer N_2 densities, which means the measurement of N_2 is made in mass channel

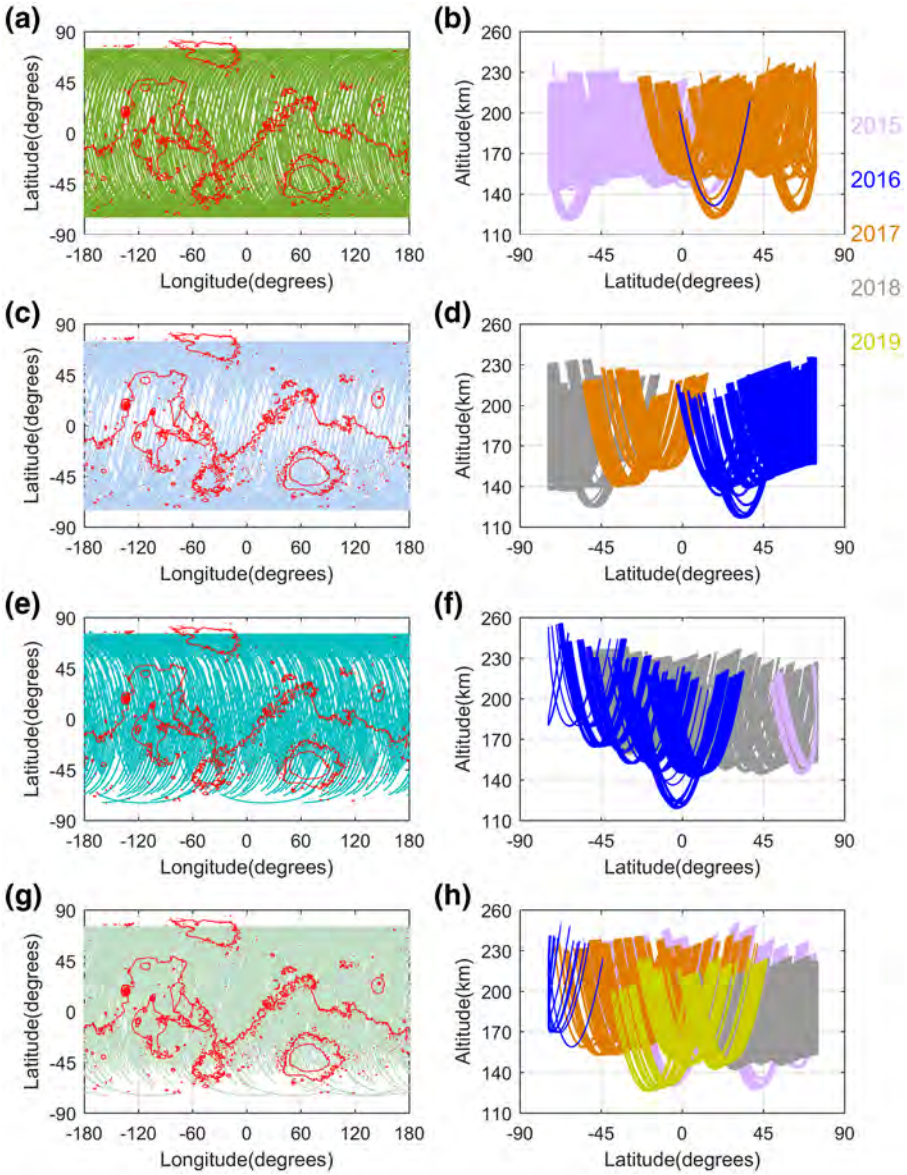

Figure 1. Data coverage of this study. In each of the panels, a small dot has been plotted at the location of every sample of data made by accelerometer. Upper to bottom panels: spring to winter refer to northern hemisphere. The coverage in (a, c, e, and g) as a function of longitude and latitude. The coverage in (b, d, f, and h) as a function of latitude and altitude above the areoid. The color-coding corresponds to data taken within the year listed (2015–2019). Topographic map is also illustrated.

14 instead of channel 28 and can be used to correct the mass channel 28 where only CO is left. Likewise, CO can break up into C and O leaving signatures in those respective channels as well which means larger error bars than other species with a similar density can be assumed. Mahaffy et al. (2015) indicated that the instrument is designed to realize substantially higher sensitivity than a nominal sensitivity of $>10^{-3}$ (counts/sec)/(part/cc) for nitrogen. Although N_2 is not included here, the general trend of CO between changes during dust storms and altitudes is effective and in line with our expectations. This study used the neutral gas density in the Martian upper thermosphere obtained by NGIMS from the public archives for nearly three Mars Years (MY32, MY33, and MY34; Earth date: from February 11, 2015 to February 28, 2019) (https://lasp.colorado.edu/maven/sdc/public/pages/datasets/ngims.html). Parts of the spatial and temporal coverage of NGIMS observations are similar with Figure 1. Here, we mainly focus on the hIGWs locating between 160

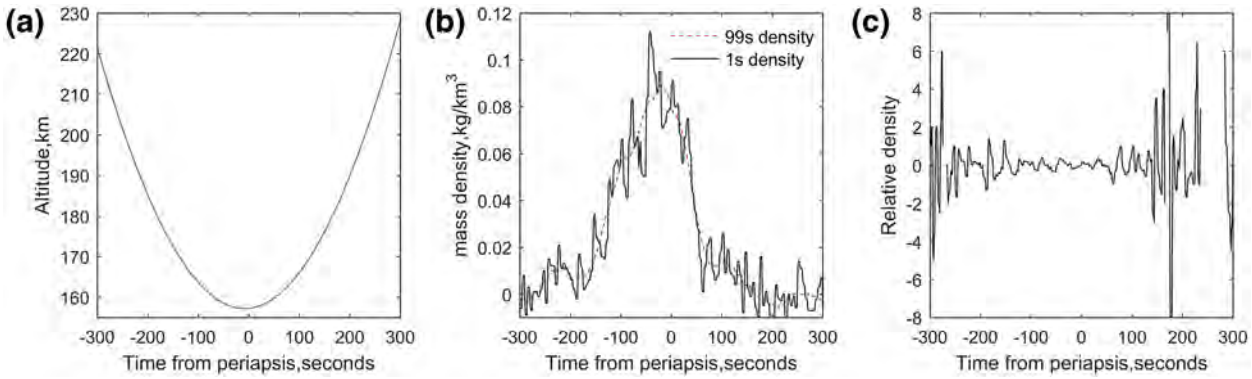

Figure 2. Data above is taken from an example orbit of 6812 from MAVEN/ACC, Periapsis location: −66.5° latitude, 282.3° longitude, 15.5 LST, 152.1° Ls. From the left to the right: orbit's trajectory characterized by the displacement in altitude along the time from periapsis in seconds; Density variations in kg/km^3 in function of the time from periapsis in seconds, red line is the 99-s density, which is assumed to be the background profile, black solid line is 1-s density; Relative density variation in time from periapsis in seconds. ACC, accelerometer; MAVEN, Mars Atmosphere and Volatile EvolutioN.

and 250 km for two main reasons: 1) the altitude from 100 to 160 km has been covered by the ACC-derived measurements (Liu et al., 2019), and 2) the density of atomic oxygen (O) surpasses the CO_2 abundance at the altitude of 220–230 km, which has been investigated by formal research (Bougher et al., 2015b). Therefore, the results of the two sensors can be compared with each other and the behavior difference between O and CO_2 can be illustrated in the transition altitude.

2.2. Methods of hIGWs Estimation

2.2.1. Gravity Waves Estimation From NGIMS Data

In order to capture the annual harmonic density cycle, Zurek et al. (2017) reported a parametric fit as follows:

$$\ln\left(\rho_{\text{mass}}\right) = p_1 + p_2 \cos\left(\text{SZA}\right) / r_{sm}^2 + p_3 / r_{sm}^2 \tag{1}$$

where ρ_{mass} represents normalized density at certain altitude, r_{sm} represents the distance between the Sun and Mars in astronomical unit (AU), cos (SZA) is the cosine of the solar zenith angle (SZA). p_1,p_2, andp_3 are parameters needed to be fit. The model is verified to fit well with MAVEN data. The three terms on the right of the equation represent constant, the flux attenuation from the Sun to Mars and the obliquity evolution of Mars, respectively. However, Liu et al. (2019) reveal that the surface dust activities play a key role in the annual cycle variations. Therefore, the model noted above may be inadequate in explaining the nonharmonic part of the dust seasons. An improved model with dust storm term proposed by Liu et al. (2019) is applied here, which can reasonably fit the annual cycle as follows:

$$\ln\left(\rho_{\text{mass}}\right) = p_1 + p_2 \cos\left(\text{SZA}\right) / r_{sm}^2 + p_3 / r_{sm}^2 + p_4 \text{Dust}_{\text{IR-CDOD}} \tag{2}$$

where p_4 represents the dust parameters, which can respond well to the global dust storm on Mars, but it seems not ideal for nonglobal dust storms. Overall, it can play a role in detrending. The model is proved to be capable of better explaining the density increase in Martian thermosphere during dust seasons (Liu et al., 2019). Consequently, we use this model to capture the density structure to achieve the purpose of detrending and calculate hIGWs. In this study, we mainly focus on the four gases detected by NGIMS, including Ar, CO_2, CO, and O. According to Jakosky et al. (2017), Ar, which is chemically inert, is weakly affected by solar photolysis and can be used to assess the upper atmospheric sputtering loss. Ar and CO_2 have very similar atmospheric density structures (Bougher et al., 2015b). Atomic oxygen O and CO are CO_2 derivatives (McElroy & Hunten, 1970), and their density is significantly affected by the thermospheric photochemical reactions (Bougher et al., 2015b). However, the intersection of the density of O and CO_2 occurs at an altitude

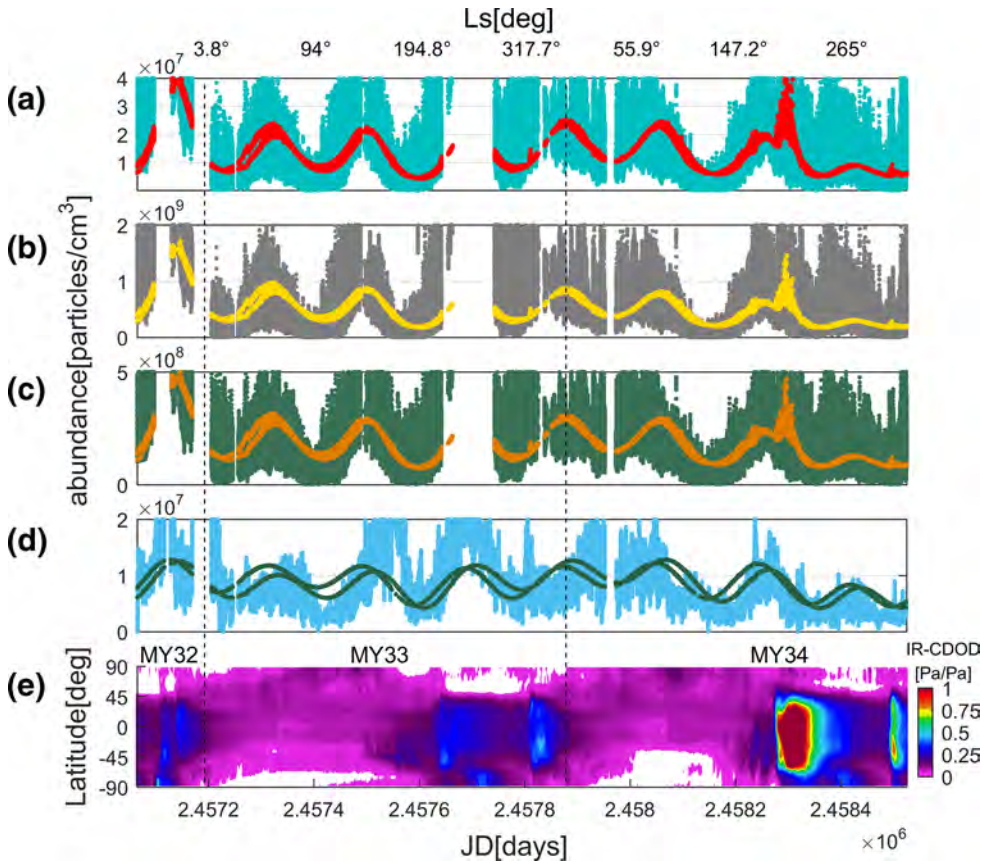

Figure 3. Panels (a, b, and c) show the fitting results of Ar, CO_2, and CO at 160 km based on the four-parameter model, respectively. Panel (d) show the fitting results of O at 220 km based on the formula proportional to cos (SZA). Dust index in (e) is represented by Infrared-Column Dust Optical Depth (Montabone et al., 2015). The solar longitude value corresponding to the Julian day is added to the *x*-axis label. SZA, Solar Zenith Angle.

of about 220 km (Bougher et al., 2015b), which indicates that the solar heating effect becomes decisive at this altitude and above. Liu et al. (2019) have reported that the IGWs are capable of extending to higher altitudes even beyond 200 km. Therefore, for the density fitting of atomic O, we use the equation proportional to cos (SZA) with altitudes limited between 220 and 250 km, expressed by

$$\rho_{\text{mass}} = a * \cos\left(\text{SZA}\right) + b \tag{3}$$

where a and b are the parameters needed to be fit, and cos (SZA) is the cosine of the SZA. The other three gases (CO_2, CO, and Ar) are fitted by four parameter model (i.e., Equation 2). The background density ρ_m is extracted by above models after the outliers are filtered (Figure 3). Then, perturbations are determined by subtracting the background profile from the instantaneous density ρ_i and normalizing by the background profile (ρ_i-ρ_m/ρ_m).

2.2.2. Gravity Waves Estimation From ACC-Derived Density

The abstraction of gravity waves from ACC-derived density is to extract atmospheric perturbations from the background. In this study, we take two different approaches to extract hIGWs from ACC-derived density in order to compare the results. Considering the response of ACC-derived density to dust storms, one of the methods is to apply the model as illustrated by Equation 2 so that we can compare it with the hIGWs obtained from neutral gases in NGIMS. Another method is similar to the one used for analyzing hIGWs in the Martian upper thermosphere by Vals et al. (2019), which is to subtract the mean density ρ_m [99-s averaged

density, background] from the instantaneous density ρ_i (1-s samples). The relative density perturbation $\delta\rho_r$ is obtained as follows:

$$\delta\rho_r = \frac{\rho_i - \rho_m}{\rho_m} \tag{4}$$

An example of orbit trajectory, residual and relative density variations for MAVEN orbit 6812 obtained from the solution described above is shown in Figure 2. The 99-s average density can provide an acceptable estimate of the "background" atmospheric state. Owing to these rather short wavelengths, atmospheric perturbations analyzed here are mainly considered as IGWs (Liu et al., 2019; Siddle et al., 2019; Terada et al., 2017).

3. Results and Analysis

3.1. Fitting Results From NGIMS

Figure 3 shows the fitting results from NGIMS. The first four panels show the fitting results of Ar, CO_2, CO at 160 km and O at 220 km respectively. The last panel illustrates the corresponding dust storm activities. In order to separate neutral gas density and the fitting curve, we expressed them in different colors. The curves are the fitting result of the model used for the specific neutral gas, and the dotted distribution represents the abundance of gases at different altitudes. The IR-CDOD data set can be found at http://www-mars.lmd.jussieu.fr/mars/dust_climatology/index.html during MY24 to MY33.

Combining the fitting coefficients and goodness illustrated in Table 1, the fitting goodness is unstable due to the influence of data coverage at altitudes from 130 to 150 km which can be seen in Ar, CO_2, and CO. The value of R-squared is bigger at 140 km than that in 130 and 150 km. Therefore, we mainly focus on hIGWs from 160 to 190 km, where the fitting goodness is better and results are more reliable. However, in the case of O, we find the value of R-squared decreases with altitudes, so we limit the range of O to 220–250 km. Liu et al. (2019) showed the parametrized model at 150 km based on different ACC data, however the fitting parameters are different from these shown in the present study, which can be expected because of the different data sources.

In addition, another interesting phenomenon has attracted our attention, that is, the inbound and outbound of SZA appear in seasonal changes, which is more obvious in Figure 3d, although this can be found in all four gases. In this study, we do not distinguish hIGWs between inbound and outbound, but focus on the hIGWs characteristics at specific altitude.

3.2. hIGWs Variations From ACC

Figure 4 illustrates hIGWs amplitudes with altitudes ranging from 160 to 180 km. We have used two different fitting results as the background densities, one is the fitting density based on Equation (2), the other is the 99-s density data. Then, the absolute value of the relative density perturbation defined by equation (4) are calculated to obtain hIGWs. In addition, for the convenience of comparison with dust storm activities, the global distribution of IR-CDOD values through three different MYs are illustrated in Figure 4 corresponding to the time of Julian Day (JD) from (a to c) showed above.

In general, hIGWs amplitudes obtained by both methods increase with altitude and changes significantly with seasons during long time scales in Figure 4, which is in agreement with what Fritts et al. (2006) found in MGS and ODY erobraking data. As illustrated in the bottom panel of Figure 4, the dust activities are more active in autumn and winter compared to spring and summer. Consequently, it is obvious to observe strong hIGWs responses to the dust storms in autumn and winter by comparison. The red dotted line in MY 34 indicates the beginning of a dramatic increase in the dust storm, the corresponding hIGWs also expand significantly, and as the dust storms weaken, the amplitude also returns to a smaller level. A similar situation can be seen in MY 33, but the dust storm activity is not strong and the amplitude only increases slightly. Due to the limitation of start time of the MAVEN mission, we are unable to obtain hIGWs for the whole MY 32.

Table 1
Model Fitting Coefficients of Four Gases at Different Altitudes

$$\ln(\rho_{mass}) = p_1 + p_2\cos(SZA) / r_{sm}^2 + p_3 / r_{sm}^2 + p_4 Dust_{IR\text{-}CDOD}$$

Ar	130 km	140 km	150 km	160 km	170 km	180 km	190 km
p1	19.90	16.08	16.32	15.75	14.23	13.02	11.21
p2	0.84	2.31	1.16	2.20	3.32	4.57	5.63
p3	−0.93	2.65	0.99	0.93	2.18	2.62	4.44
p4	3.53	4.70	0.82	0.55	0.96	1.19	1.35
RMSE	4.74e8	9.06e7	1.98e7	1.02e7	7.50 e6	5.31e6	1.45e7
SSE	5.84e21	6.46e20	9.55e19	3.88e19	1.72e19	6.98e18	4.70e19
R^2	0.04	0.37	0.02	0.17	0.20	0.21	0.01
			CO_2				
p1	23.47	19.51	19.90	18.61	16.75	15.24	13.65
p2	1.29	2.81	1.16	2.08	3.42	4.71	5.12
p3	−0.32	3.20	1.17	2.71	4.51	5.47	6.90
p4	3.09	4.84	0.55	0.47	0.98	1.24	1.33
RMSE	2.29e10	4.89e9	9.40e8	4.34e8	3.29e8	2.15e8	1.15e8
SSE	1.38e25	1.89e24	2.12e23	6.79e22	3.22e22	1.10e22	2.52e21
R^2	0.06	0.38	0.03	0.19	0.23	0.24	0.16
			CO				
p1	22.01	18.57	18.53	18.17	16.88	15.92	15.11
p2	1.31	2.08	0.92	1.79	2.58	3.47	3.86
p3	−0.22	2.85	1.90	1.53	2.70	3.13	3.29
p4	2.21	3.93	0.57	0.38	0.68	0.85	0.94
RMSE	5.21e9	9.498e8	2.07e8	1.16e8	8.94e7	6.43e7	3.93e7
SSE	7.10e23	7.10e22	1.03e22	4.83e21	2.38e21	9.95e20	3.03e20
R^2	0.03	0.38	0.05	0.18	0.23	0.31	0.28

$$\rho_{mass} = a * \cos(SZA) + b$$

O	220 km	230 km	240 km	250 km	260 km	270 km	280 km	290 km
a	4.32e6	3.08e6	2.35e6	1.86e6	1.48e6	1.14e6	8.94e5	7.46e5
b	8.52e6	6.74e6	5.57e6	4.74e6	4.13e6	3.63e6	3.18e6	2.85e6
RMSE	4.91e6	3.71e6	2.89e6	2.30e6	1.88e6	1.58e6	1.35e6	1.16e6
SSE	2.77e18	1.30e18	6.36e17	3.15e17	1.60e17	8.16e16	4.20e16	2.02e16
R^2	0.17	0.15	0.14	0.13	0.11	0.08	0.06	0.05

However, it can be predicted that the changes of hIGWs in MY 32 are affected by dust storms. Therefore, the impact of dust storms on hIGWs is decisive.

Liu et al. (2019) reveal that the apparent amplitude of the gravity waves at a fixed altitude decreases as the density increases on this condition. The very good agreement in ACC hIGWs gives us great confidence in the method used. The dependence is clearer at higher altitudes due to more coverage. Since the altitude of periapsis during MAVEN primary science mission is about 150 km, which is lowered to about 120 km during Deep Dip campaigns (Zurek et al., 2017), dotted distributions are fewer between 120 and 150 km. Therefore, the perturbations at lower altitudes are not included in this study. By considering the conservation of momentum in a conservative atmosphere, Siddle et al. (2019) give the reason why the amplitudes are

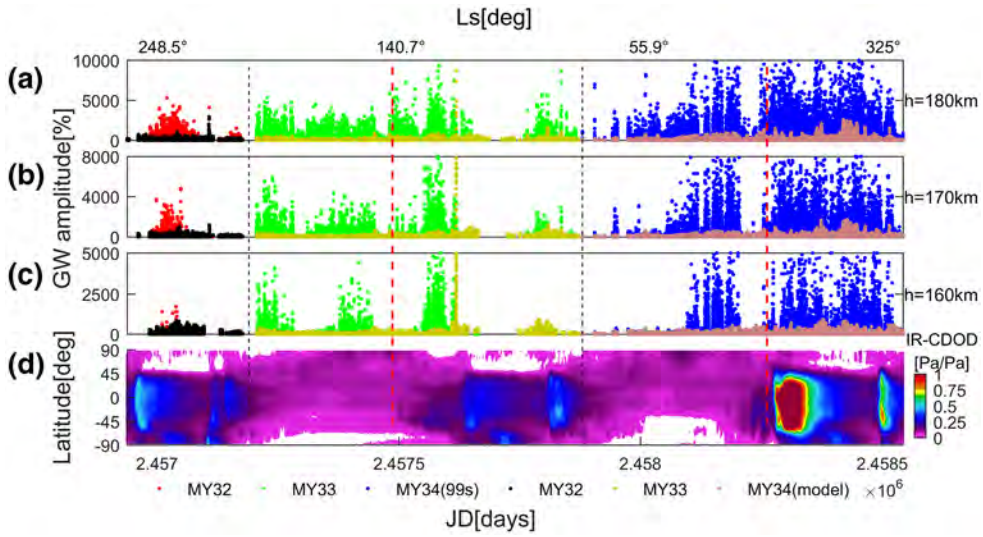

Figure 4. Interannual variability of hIGWs amplitudes measured by MAVEN/ACC. Each point corresponds to the sampling of each orbit at a certain location. In this figure, each point is normalized to a constant reference altitude from (a) 180 to (c) 160 km. The variations of hIGWs using 99s density and model-fitted background profiles are expressed in six different colors in 3 MYs. The color map in (d) shows the 9.3 μm absorption column dust optical depth normalized to the reference 610 Pa pressure level. Data gathered from MY 32 to MY 34 are in red, green, and blue, respectively. The dashed red lines mark the obvious responses of hIGWs to dust storms. Least squares algorithm is used. The solar longitude value corresponding to the Julian day is added to the *x*-axis label. ACC, accelerometer; hIGWs, horizontal internal gravity waves; MY, Martian Year; MAVEN, Mars Atmosphere and Volatile EvolutioN.

expected to increase exponentially with altitude as the density decreases, thus explaining the phenomenon presented here.

Owing to the increase of gravity wave amplitude with altitude, large departures of density, temperature and winds in the thermosphere can be caused by the upward propagation of gravity waves from their tropospheric sources to the upper atmosphere. Based on the IR-CDOD data given by Montabone et al. (2015), it can be known that the autumn and winter dust storms in MY 32 approximate to those in MY 24, and the dust storm activity in MY 33 is extremely inactive, which is one of the most inactive years of dust storm activity happened on Mars since the record. The phenomenon shown in Figure 4 is consistent with the fact described above. The comparison is not obvious in MY 32 because of incomplete data coverage. However, comparing the hIGWs in MY 33 and MY 34, the amplitudes in MY 34 are larger at the same altitudes from 160 to 180 km.

According to the hIGWs obtained from 99s-averaged density, the overall amplitude increased significantly from 160 to 180 km by approximately two times. As far as the response to dust storms is concerned, the amplitude variation in dust seasons are only obvious in MY 34. Due to overfitting, the response was weakened in MY 33. However, the hIGWs obtained by the model are completely different. The amplitudes obtained from the model are much smaller than that of 99-s averaged density as background profile. From a trend point of view, the amplitude varies significantly with the dust storms, especially in MY 34, which is more in line with the actual conditions of the Martian atmosphere. Although the dust storms are inactive in MY 33, we can still see a clear response of hIGWs. Consequently, it can be easily concluded that the model can better capture the density structure, which is consistent with the results in the work of Zurek et al. (2015).

Figure 5 shows the normalized perturbations obtained from Equation 4. σ_1 and σ_{99} represent the derived errors of ACC 1-s density and 99-s density, respectively. Of the three MYs shown above, the hIGWs in dust seasons in MY 34 have the strongest amplitude, and the corresponding error fluctuations also show the same characteristics, which means that the regions with large error fluctuations are accompanied by strong dust activities and the phenomenon is more obvious in MY 34. Starting from the time indicated by the red dotted line, accompanied by increased dust storm activities, the error fluctuation amplitude has been in an

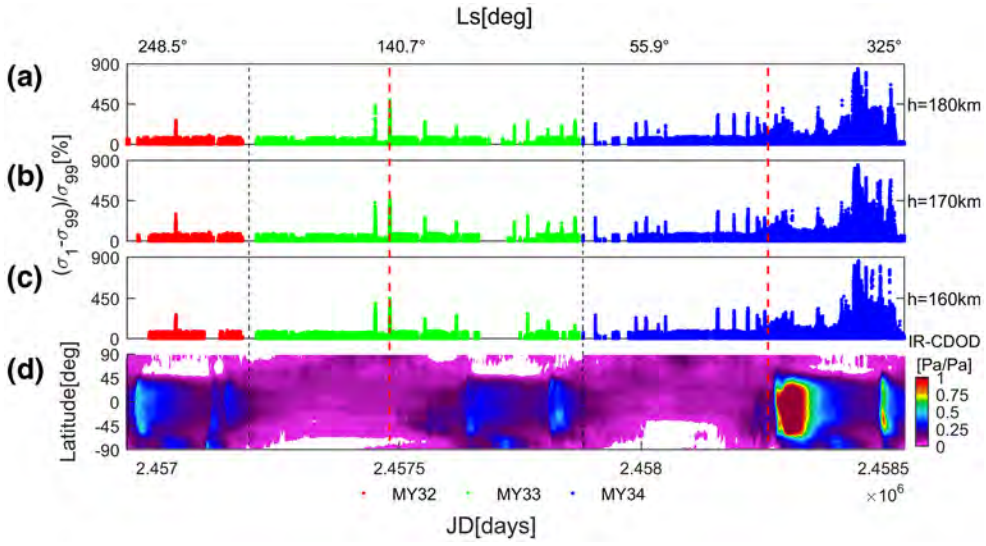

Figure 5. Interannual variability of $(\sigma_1-\sigma_{99})/\sigma_{99}$ measured by MAVEN/ACC. Each point corresponds to the sampling of each orbit at a certain location. In this figure, ach point is normalized to a constant reference altitude from (a) 180 to (c) 160 km. The color map in (d) shows the 9.3 μm absorption column dust optical depth normalized to the reference 610 Pa pressure level. Data gathered from MY 32 to MY 34 are in red, green, and blue, respectively. The dashed red lines mark the obvious responses of hIGWs to dust storms. Least squares algorithm is used. The solar longitude value corresponding to the Julian day is added to the *x*-axis label. ACC, accelerometer; hIGWs, horizontal internal gravity waves; MY, Martian Year; MAVEN, Mars Atmosphere and Volatile EvolutioN.

irregular state with significant peaks from 160 to 180 km. However, the significantly smaller perturbations in MY 32 and 33 correspond to inactive dust storm activities. After the time indicated by the red dotted line in MY 33, the frequency of error fluctuations increases, and the dust storm is still considered to be the cause. In the nondust storm season, the amplitudes are not large and tend to be stable. Only in MY 34, there are some large ups and downs that may be caused by the early peak of the dust storm, which may indicate a large-scale global dust storm.

3.3. hIGWs Varations From NGIMS

The perturbations of Ar and CO_2 in the thermosphere are almost identical as shown in Figures 6 and 7, which is consistent with the results found in England et al. (2016b). Moreover, in MY 33 and 34, the hIGWs also increase significantly with expended dust storms. However, according to the hIGWs in MY 34, we observe that the amplitude didn't increase significantly during the dust storms, but was the highest in the intermittent period of dust storms between the autumn and winter (a kind of time lag). Our understanding is as follows: when the dust storm occurs, the atmosphere is lifted to upper layers under the influence of the dust storm, then the background density increases and the amplitude decreases. After the dust storm, the amplitude will increase as the background density decreases. This is the reason why the peaks in MY 34 in Figures 6 and 7 appear after the dust storms in autumn but before winter.

In addition, when comparing with the hIGWs obtained by ACC-derived densities, we can find the responses of Ar and CO_2 to the dust storms are more evident, especially when the hIGWs increases again with the existence of the late peak in MY 34. Moreover, the general perturbation trends of the two gases are consistent from the beginning to the disappearance of dust storms. This situation can be expected because Ar is chemically inert and its distribution is only affected by dynamics (Siddle et al., 2019), while the relative molecular mass of CO_2 is similar to that of Ar.

Figures 8 and 9 show the hIGWs of CO and O, the photochemical derivatives of CO_2, respectively. From the amplitudes of CO hIGWs, it can be easily observed that the amplitude has a certain degree of increasing in autumn and winter of MY 33 and 34, of which the amplitude is 2–3 orders of magnitude higher from 180

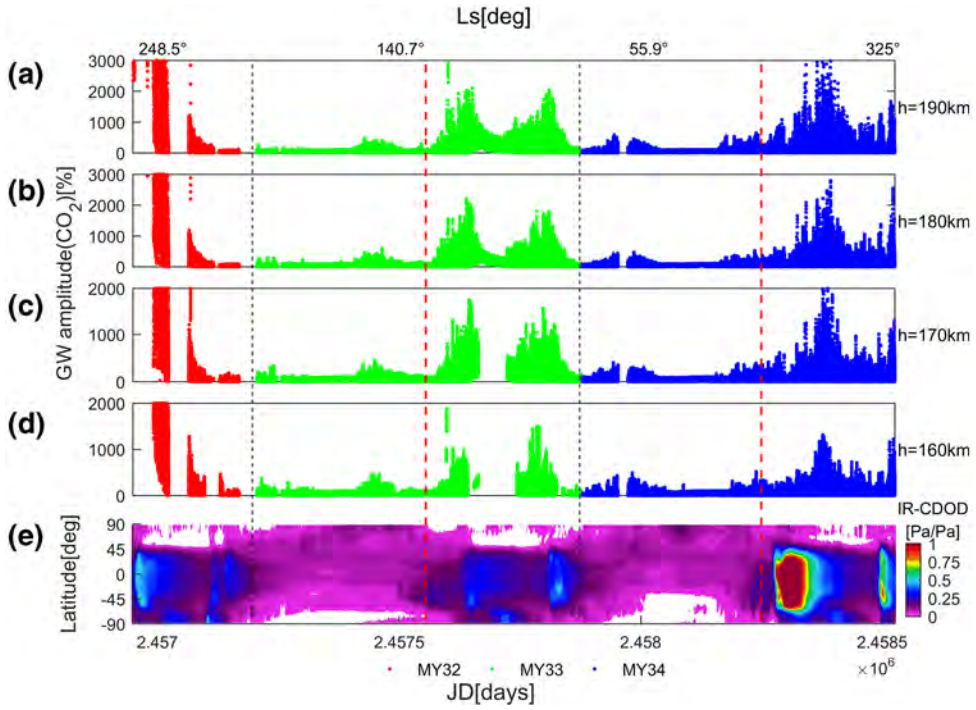

Figure 6. Interannual variability of hIGWs amplitudes of CO_2 measured by MAVEN/NGIMS. Each point corresponds to the sampling of each orbit at a certain location. In this figure, each point is normalized to a constant reference altitude from (a) 190 to (d) 160 km. The color map in (e) shows the 9.3 μm absorption column dust optical depth normalized to the reference 610 Pa pressure level. Data gathered from MY 32 to 34 are in red, green, and blue, respectively. The dashed red lines mark the obvious responses of hIGWs to dust storms. Least squares algorithm is used. The solar longitude value corresponding to the Julian day is added to the *x*-axis label. hIGWs, horizontal Internal Gravity Waves; MY, Martian Year; MAVEN, Mars Atmosphere and Volatile EvolutioN; NGIMS, Neutral Gas and Ion Mass Spectrometer.

to 190 km than the nondust storm season. At other times, the perturbations are relatively flat, which shows the situation without the impact of dust storms. Despite the small amount of data coverage in MY 32, a dramatic change in amplitude in MY 32 is observed.

By comparing the fluctuations of CO and CO_2, we find they are somewhat similar. The annual changes of CO appear to show a characteristic that follows the trend of CO_2. They all have an obvious response to the surface dust storms in autumn and winter but there is a difference. As the altitude increases, the amplitude in CO hIGWs increases slightly slower compared to that in CO_2. However, with the increasing altitudes, the peaks of the waves appear at the same position and the basic waveform remains unchanged, although the peaks of hIGWs in CO are not as large as that in CO_2.

However, the hIGWs variations of atomic O are very special as shown in Figure 9. As one of the derivatives of CO_2, the Sun plays a leading role in shaping the atomic O structure in the thermosphere (Cravens et al., 2017; Terada et al., 2017). Among them, photodissociation occupies an important part, and related series of chemical reactions play an auxiliary role (Lefèvre & Krasnopolsky, 2017). In contrast, dust storms have little effect on the O hIGWs amplitude. The amplitude does not change significantly with the appearance of large-scale dust storms in MY 34. Leclercq et al. (2018) used O and other density data to simulate how perturbations propagate through the transition region from a collision dominated atmospheric state in which the perturbations are produced to the ballistic regime, where particles do not have enough escape energy to cross the upper boundary. They concluded that the amplitudes at Mars decrease eventually at altitudes well above the nominal exobase, which is consistent with the phenomenon shown here that the amplitude range of atomic O in Figure 9 decreases with increasing altitudes as well. Here, we limit the research

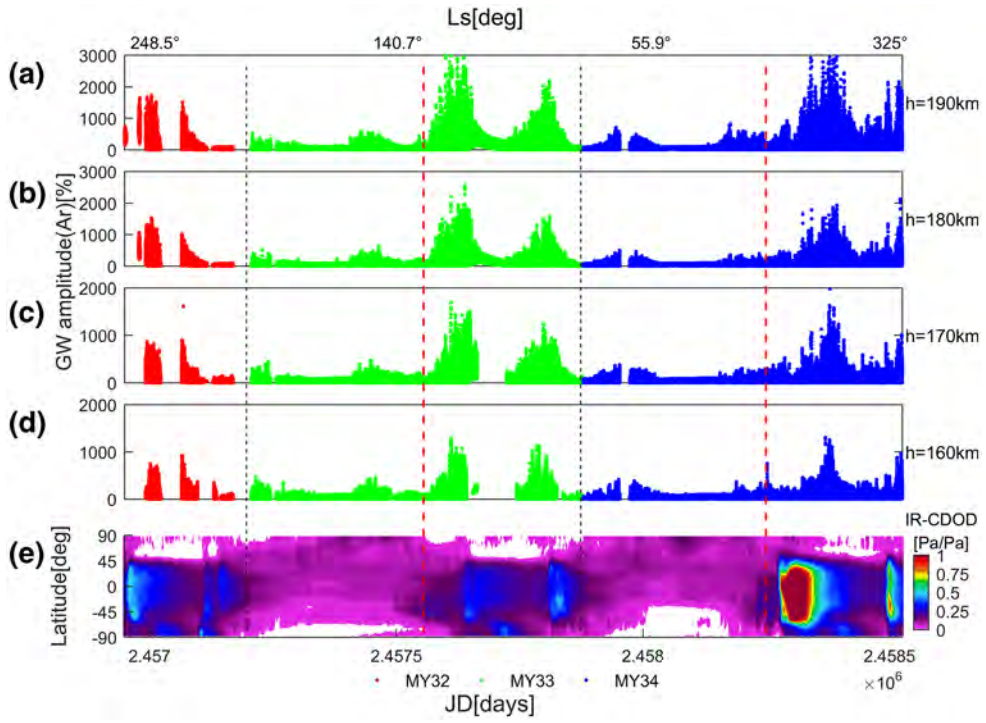

Figure 7. Interannual variability of hIGWs amplitudes of Ar measured by MAVEN/NGIMS. Each point corresponds to the sampling of each orbit at a certain location. In this figure, each point is normalized to a constant reference altitude from (a) 190 to (d) 160 km. The color map in (e) shows the 9.3 μm absorption column dust optical depth normalized to the reference 610 Pa pressure level. Data gathered from MY 32 to 34 are in red, green, and blue, respectively. The dashed red lines mark the obvious responses of hIGWs to dust storms. Least squares algorithm is used. The solar longitude value corresponding to the Julian day is added to the *x*-axis label. hIGWs, horizontal internal gravity waves; MY, Martian Year; MAVEN, Mars Atmosphere and Volatile EvolutioN; NGIMS, Neutral Gas and Ion Mass Spectrometer.

altitude of O hIGWs to between 220 and 250 km in the exosphere, which has gone beyond the thermosphere (Leclercq et al., 2018; Terada et al., 2017). This give further reasoning to the result of O.

However, we still notice that there is an abnormal peak between summer and autumn in MY 33, which does not correspond to the time range of dust storms. Medvedev and Yiğit (2019) reported that neutrals are perturbed as IGWs propagate through the thermosphere, during which ions are influenced too. The phenomenon presented here could be large scale traveling ionospheric disturbances (TIDs) of electron density, which could be response to the passage of GWs.

4. Discussion

Gravity waves have vertical and horizontal components. MAVEN's orbit is tilted and most of the time contains two components at the same time, although the spacecraft is moving almost horizontally close to periapsis. The obtained spatial spectra based on MGS and ODY ACC data are believed to represent horizontal spectra of density perturbations, which is the key to defining perturbations as horizontal components (Creasey et al., 2006; Fritts et al., 2006). Additionally, the observations obtained from NGIMS data in England et al. (2016b) also follow the universal spectrum well, which means the apparent wavelength can be a reasonable proxy for the true horizontal wavelength. Consequently, we classify the range of 5 km above and below a specific altitude to that reference altitude and calculate its perturbations, which are interpreted as hIGWs.

GW amplitude represents short-to long-term changes. Horizontal components of IGWs vary with altitude, but the degree is much smaller than their vertical and temporal scales.

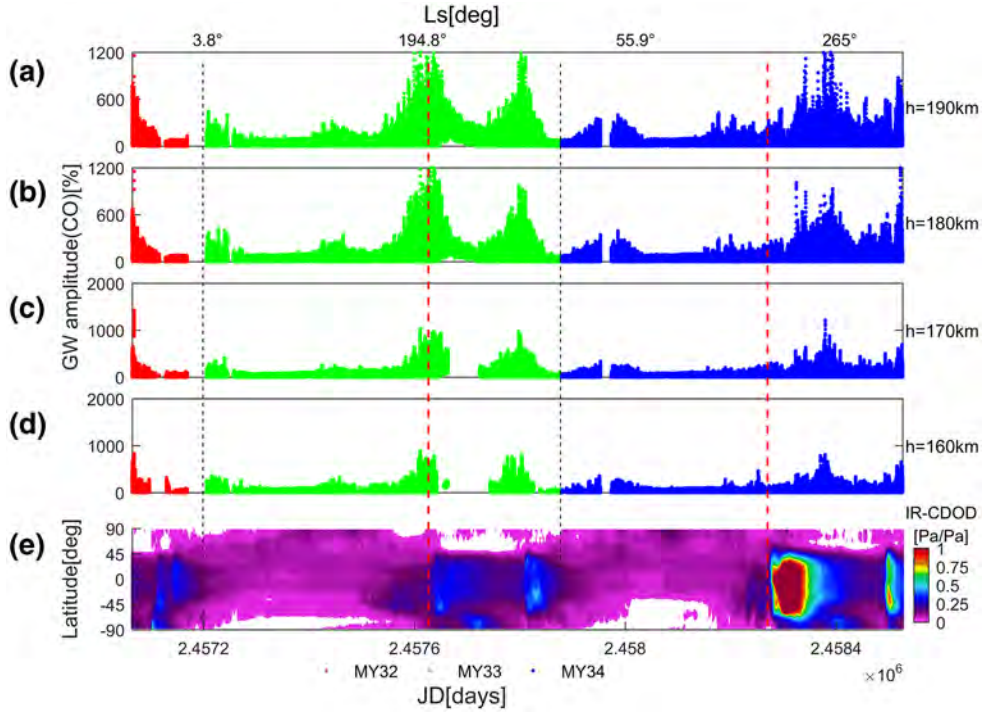

Figure 8. Interannual variability of hIGWs amplitudes of CO measured by MAVEN/NGIMS. Each point corresponds to the sampling of each orbit at a certain location. In this Figure, each point is normalized to a constant reference altitude from (a) 190 to (d) 160 km. The color map in (e) shows the 9.3 μm absorption column dust optical depth normalized to the reference 610 Pa pressure level. Data gathered from MY 32 to 34 are in red, green, and blue, respectively. The dashed red lines mark the obvious responses of hIGWs to dust storms. Least squares algorithm is used. The solar longitude value corresponding to the Julian day is added to the *x*-axis label. hIGWs, horizontal internal gravity waves; MY, Martian Year; MAVEN, Mars Atmosphere and Volatile EvolutioN; NGIMS, Neutral Gas and Ion Mass Spectrometer.

However, it has been indicated that IGWs originating from the lower atmosphere propagate to F region altitudes, where appreciable dynamical effects are produced (Yiğit et al., 2012; Yiğit & Medvedev, 2010). In additional, the mean zonal GW drag constitutes the main part of the mean effects and the mean effects in the thermosphere are larger than the ones in the mesosphere and the lower thermosphere (MLT). Consequently, the effects of horizontal gravity waves in the thermosphere cannot be ignored.

4.1. Seasonal Variations of hIGWs From ACC

In order to further explore the seasonal variations of hIGWs, perturbations in four seasons at 160 km obtained by the four-parameter model are illustrated in Figure 10 with the topography map superposed to compare with the hIGWs amplitudes. In general, there is no possible correspondence between the hIGWs observations and Mars's topography found here, especially in the case of undulating terrain in the southern hemisphere. There are many factors that can trigger gravity waves, such as topography, dust storms, etc. Siddle et al. (2019) reveal that waves remain constant between two different altitudes in similar regions with no correlation between wavelength and topography to be found, consistent with the NGIMS and MGS ACC measurements (Creasey et al., 2006; Terada et al., 2017). So, here we mainly focus on the influence of dust storm on hIGWs.

In Figure 10, the similar longitudinal dependence (e.g., Terada et al., 2017) is recognized, which is still unclear. In addition, Terada et al. (2017) pointed out that some evident seasonal variations caused by the orbital bias of MAVEN happened in spring and summer on Mars, similar phenomenon can also be found here, which means larger amplitude hIGWs appear in the middle latitudes in Figures 10a and 10b. As the

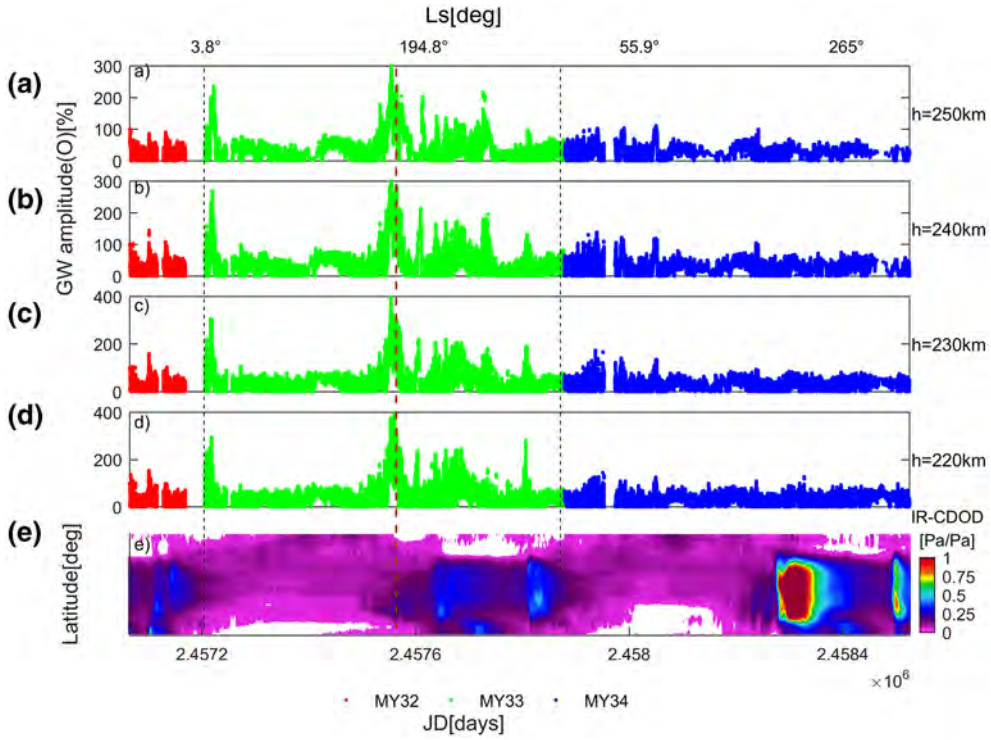

Figure 9. Interannual variability of hIGWs amplitudes of O measured by MAVEN/NGIMS. Each point corresponds to the sampling of each orbit at a certain location. In this figure, each point is normalized to a constant reference altitude from (a) 250 to (d) 220 km. The color map in (e) shows the 9.3 μm absorption column dust optical depth normalized to the reference 610 Pa pressure level. Data gathered from MY 32 to 34 are in red, green, and blue, respectively. The dashed brown line mark the obvious responses of hIGWs to dust storms. Least squares algorithm is used. The solar longitude value corresponding to the Julian day is added to the *x*-axis label. hIGWs, horizontal internal gravity waves; MY, Martian Year; MAVEN, Mars Atmosphere and Volatile EvolutioN; NGIMS, Neutral Gas and Ion Mass Spectrometer.

latitude increases in the northern hemisphere in Figure 10b, the amplitude decreases significantly with the time turns to daytime, which partly reflect the diurnal variations. Consistency with the results of Terada et al. (2017) increases our confidence in the method used.

However, the amplitude of hIGWs in Figure 10c increases sharply, which is different from the situation in Figures 10a and 10b. From the annual changes of the dust storm in Figures 3, 4–9, we observe that dust storm activities are usually centered on the equator, and the latitude range affected is related to the severity of the dust storm. However, the hIGWs amplitudes are smaller in the region centered on the equator and within the range of 30° latitude between the northern and southern hemisphere. Greater amplitude appears outside this area. In fact, when dust storms occur or reach its peak, seasonal structures of the atmosphere is affected and lifted to upper layers, which has been proved in many works (England et al., 2016b; Keating et al., 1998; Montabone et al., 2015; Rafkin et al., 2002). The background density increases during this process, and the hIGWs amplitude decreases (Liu et al., 2019; Smith, 2009). In the intermittent period of dust storms in the middle of autumn and winter or in the later period of winter dust storms, the amplitude may increase as the background density decreases, that maybe the reason why the amplitude increases near the equator in Figure 10d. This phenomenon once again shows that dust storms have an impact on the seasonal atmospheric structure of the thermosphere and the overall uplift, which has also been confirmed in the work of many people (England et al., 2016b; Keating et al., 1998; Montabone et al., 2015; Rafkin et al., 2002). Moreover, the atmospheric uplift caused by the dust storms is coupled with the gravity waves, and this process also helps the gravity waves propagate to higher layers, thereby having higher amplitudes.

In fact, during MY 34, from May 5, 2017 to March 23, 2019 on earth, a large-scale regional dust event in Mars was observed, which is global dust event (GDE). The GDE was observed to show a strong signature within

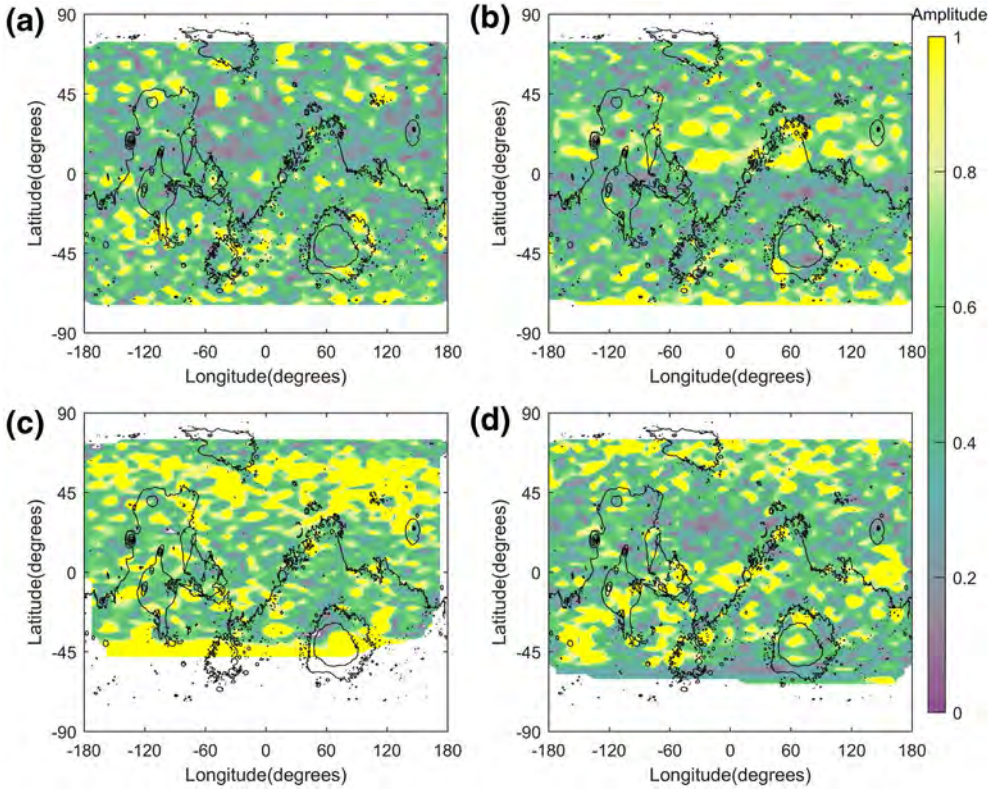

Figure 10. Longitudinal-latitudinal distributions of hIGWs from ACC-derived density obtained by the four-parameter model in four seasons at 160 km. Panel (a–d) represent spring, summer, autumn, and winter, respectively. ACC, accelerometer; hIGWs, horizontal internal gravity waves.

three days both in the dust and atmospheric temperature field, of which the zonal mean temperatures at 50 Pa exceeded the threshold of 200 k. Montabone et al. (2019) also pointed out that an extreme dust event occurred near the time of the northern autumn equinox, which consists of multiple large dust storms that have devoured all longitudes and most latitudes and lasted more than 150 Martian sols. In Figure 11, the global distribution of 9.3 μm absorption column dust optical depth normalized to the reference 610 Pa pressure level and the ACC-derived hIGWs at 160 km in four seasons of MY 34 are illustrated. We observe that dust storms in MY34 are concentrated in the equatorial region with wide global coverage (Figures 11e and 11g). However, within the area affected by the dust storms from 45°N to 45°S, we notice that hIGWs amplitude increases in some regions rather than in a larger range (Figures 11f and 11h), it seems that hIGWs amplitude decrease in other areas. For further comparison, the distributions of 9.3 μm absorption column dust optical depth normalized to the reference 610 Pa pressure level and hIGWs amplitude in MY 34 as function of solar longitude and longitude are illustrated in Figure 12. The large-scale dust storms lasted from about Ls 180°–230°, high-amplitude hIGWs are only sporadically covered during this period. However, before the occurrence of duststorms in winter from about Ls 230°–320°, large amplitudes appear in stripes and increase in range. When the dust storm occurs in winter, the amplitude decreases again and increases again after the dust storm ends. This further confirms our guesses that when the dust storms are violently active, the atmosphere is rapidly lifted and the background density increases, so that the amplitude of gravity waves decreases, which maybe the evidence that the dust storms can affect the thermosphere and further affect the hIGWs by increasing the density in the upper layer.

In addition, outside the range of dust storms in MY 34, we also observed large latitude-dependent amplitude in the mid-high latitudes in both northern and southern hemispheres (Figures 10f and 10h). However, the high-amplitude area in the southern hemisphere does not seem to be related to the terrain. In spring and summer, when dust storms are inactive, the amplitude will increase with smaller background density (Figure 12b).

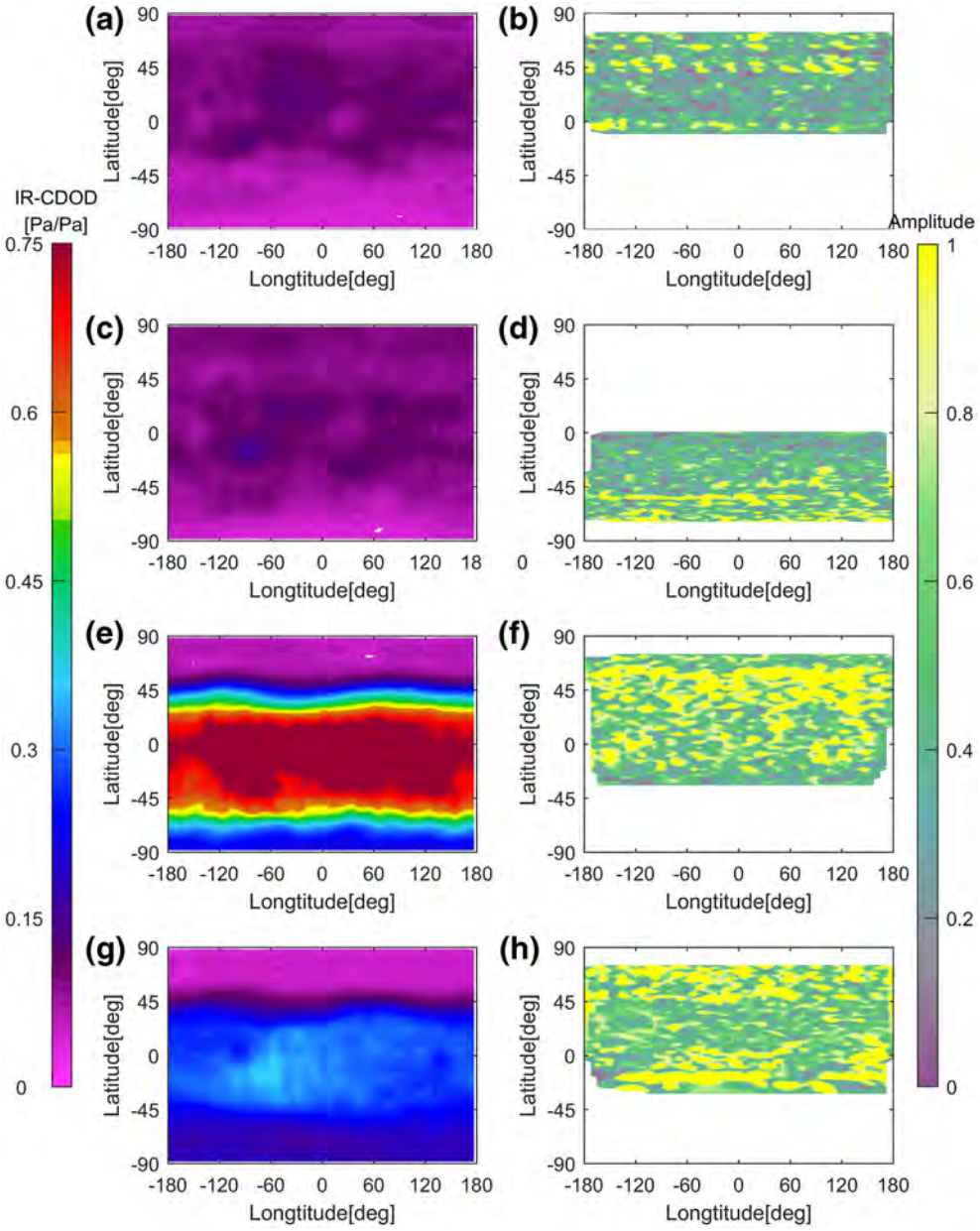

Figure 11. (Left) Longitudinal-latitudinal distributions of 9.3 μm absorption column dust optical depth normalized to the reference 610 Pa pressure level. (Right) Longitudinal-latitudinal distributions of hIGWs from ACC-derived density obtained by the four-parameter model in MY 34 at 160 km. (a and b), (c and d), (e and f), (g and h) represent spring, summer, autumn, and winter, respectively. ACC, accelerometer; hIGWs, horizontal internal gravity waves.

4.2. Seasonal Variations of CO_2 hIGWs From NGIMS

The larger hIGWs amplitude is found around 30°N in Figure 13a and in the middle latitudes in Figure 13b, which is consistent with the results in Terada et al. (2017) based on the very similar characteristics of CO_2 and Ar in the Martian atmosphere. These changes are caused by the track deviations, which have limited correlationship with the dust storms (Figures 14a, 14b, 14c & 14d). However, the variations in Figures 13c and 13d mainly reflect the impact of dust storms (Figures 14e and 14g). Note the area with low amplitudes near the equator in Figure 13c is similar to those that appeared in Figures 10c, 11f, and 14f, while the increased amplitude in Figures 13d and 14h is considered to be due to the weakening of the impact of the dust

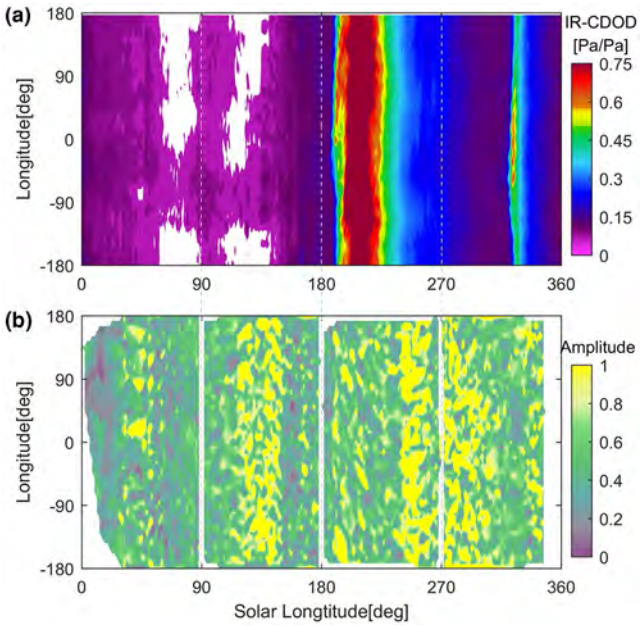

Figure 12. Panel (a) shows the distributions of 9.3 μm absorption column dust optical depth normalized to the reference 610 Pa pressure level in MY 34 as function of solar longitude and longitude. Panel (b) is the same as (a) but showing hIGWs amplitudes at 160 km. hIGWs, horizontal internal gravity waves; MY, Martian Year.

storm and the decrease in background density. Additionally, the distribution of hIGWs amplitude also indicate the influence scope of dust storms (Figures 13c, 13d, and 14f).

4.3. Seasonal Variations of O hIGWs From NGIMS

Our results indicate that O hIGWs is hardly affected by the dust storms (Figures 15e, 15f , 15g, 15h, 16c & 16d) and has nothing to do with the terrain either, especially in spring and summer when the dust storm factor can be eliminated (Figures 15a, 15b, 15c, 15d, 16a & 16b). We also notice that larger amplitude hIGWs populate near 50°N in Figure 16b, which is different from the fact that larger amplitude in CO_2 and ACC are concentrated in the area less than 45°N (Figures 10b and 13b), indicating the impact of TIDs.

We have noticed that the impact of sandstorms cannot be ignored. The PCA algorithm is used in Liu et al. (2019) work to analyze the seasonal density and a significant effect of dust storms on the annual thermosphere density cycle is found. Wu et al. (2020) have reported that dust storm activity can strongly affect the movement range of the dust fronts, even the Martian atmosphere. As described in this study, the seasonal structure of the upper atmosphere is changed due to the existence of the dust, which have been observed in this study (Figures 4 and 6–9) and other studies (England et al., 2016a; Montabone et al., 2019) as well.

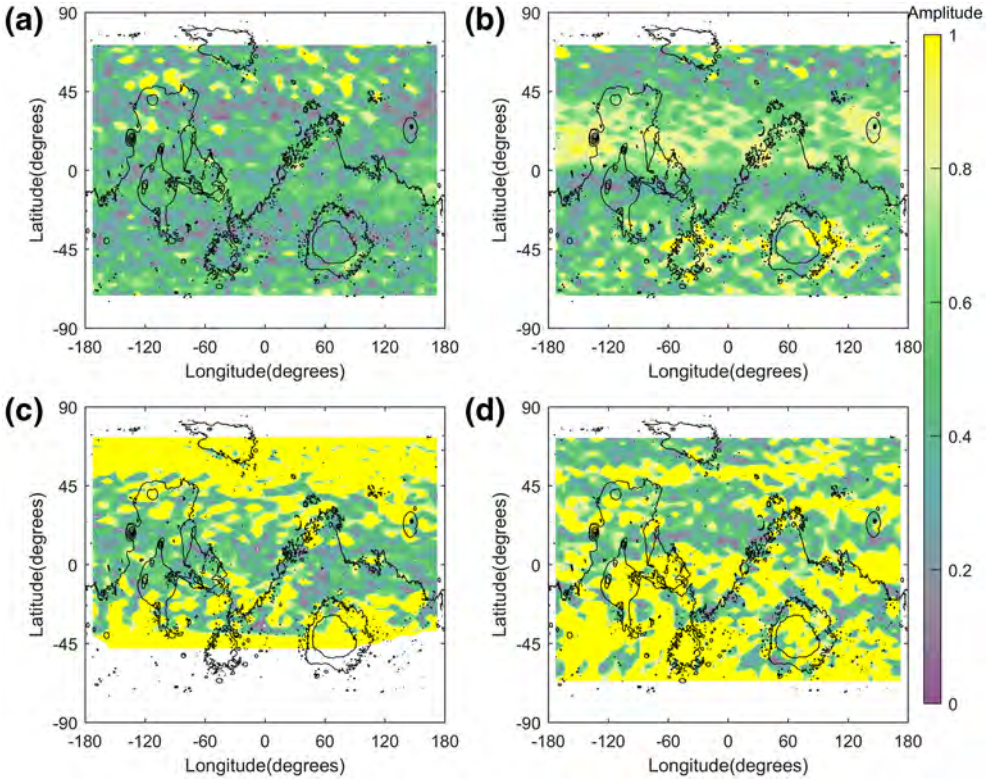

Figure 13. Same plot as Figure 10 but for CO_2 hIGWs amplitudes. hIGWs, horizontal internal gravity waves.

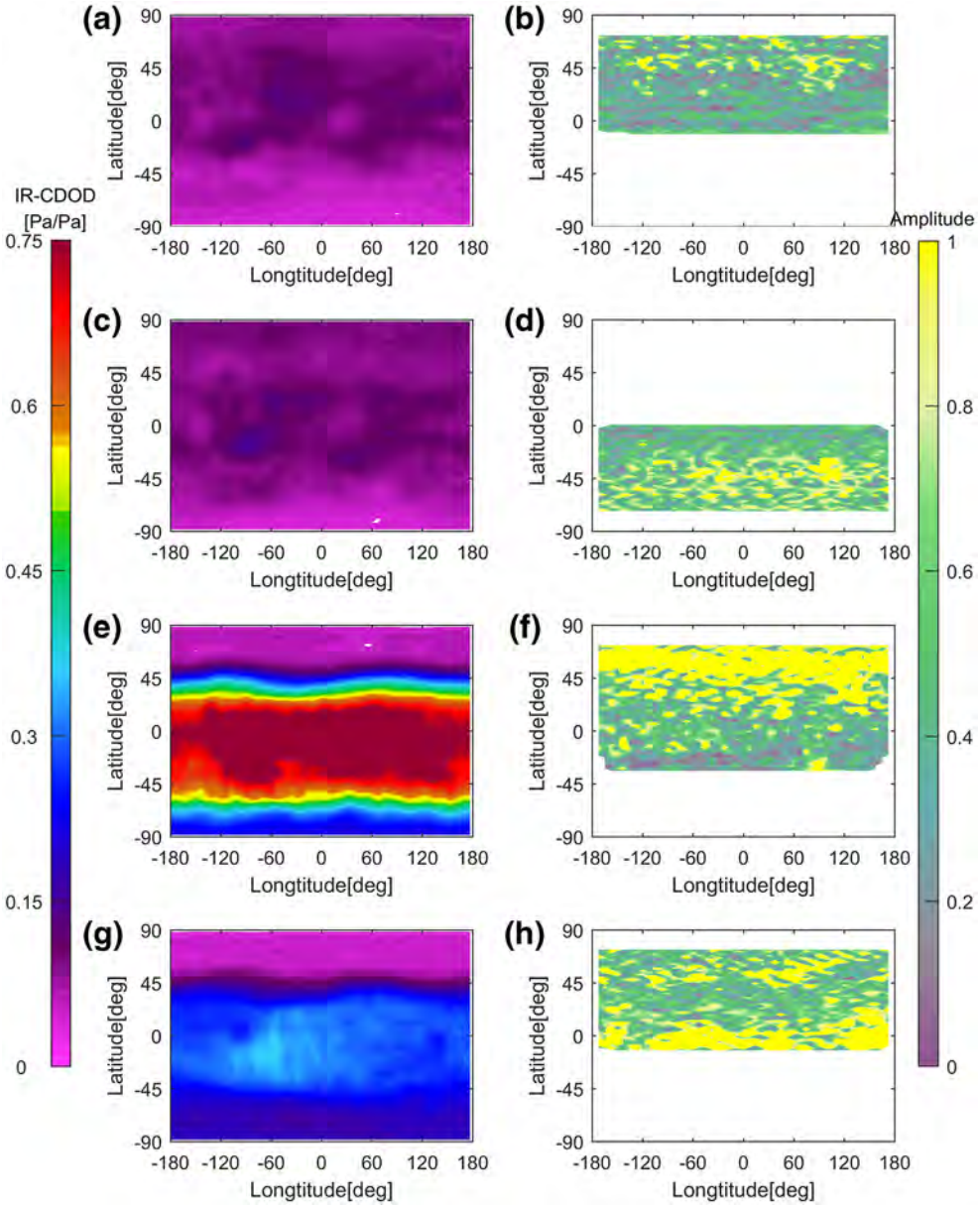

Figure 14. Same plot as Figure 11 but for CO_2 hIGWs amplitudes. hIGWs, horizontal internal gravity waves.

5. Conclusions

Horizontal IGWs are extracted and studied for the first time from the ACC-derived and NGIMS-measured densities. The results show that amplitudes appear to vary with altitudes and dust storms. Dust storms will lead to the increase of hIGWs amplitudes. In MY 32 and 33, the dust activities are not so strong compared to that in MY 34. The MY 34 is a GDE as observed by Montabone et al. (2019), in which the dust storms have a stronger influence on the hIGWs. Based on the hIGWs obtained in NGIMS measurements, we found that the perturbations of Ar and CO_2 have similar characteristics during the seasonal evolution, the general trend of which is consistent with the process of dust storms. The annual changes of CO perturbations appeared to follow the trends in CO_2, but the magnitude is much smaller. The observations show that the variations of hIGWs in these three gases are mainly controlled by dust storms. The density of atomic oxygen O in the thermosphere/exosphere is greatly influenced by solar heating and dissociation effects.

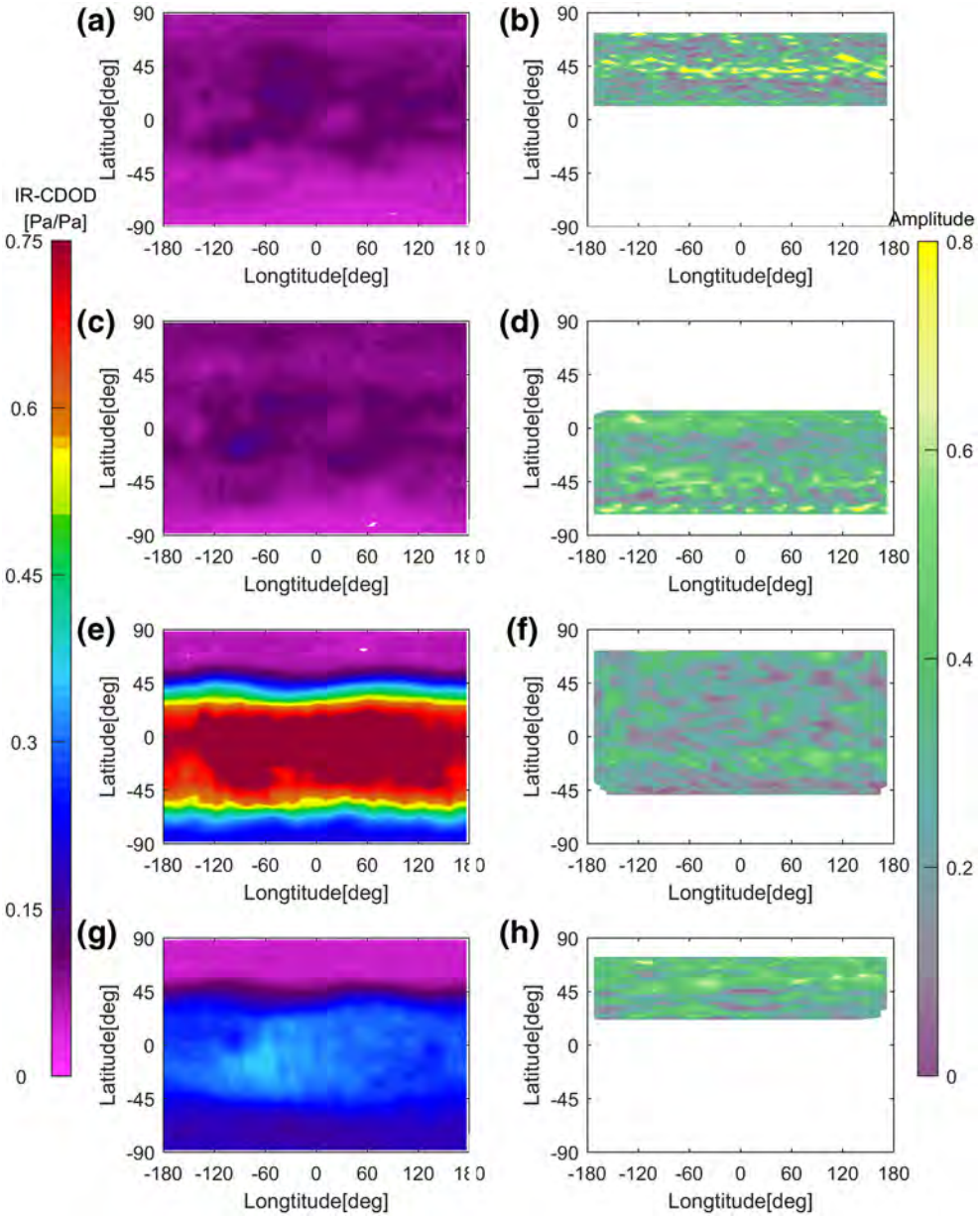

Figure 15. Same plot as Figure 11 but for O hIGWs amplitudes at 240 km. hIGWs, horizontal internal gravity waves.

However, the observed hIGWs in O are not affected by dust storms. As GWS plays an important role in the Martian atmosphere, the effects of horizontal gravity waves and dust storms cannot be ignored. This study may help improving the understanding of horizontal gravity waves and provide the means of dust storm monitoring.

Data Availability Statement

The ACC and NGIMS datasets used in this paper are available in https://atmos.nmsu.edu/PDS/data/PDS4/MAVEN/acc_bundle/l3/ and https://atmos.nmsu.edu/PDS/data/PDS4/MAVEN/ngims_bundle/l3/, respectively. The IR-CDOD dataset generated by 2015 can be found at http://www-mars.lmd.jussieu.fr/mars/dust_climatology/index.html.

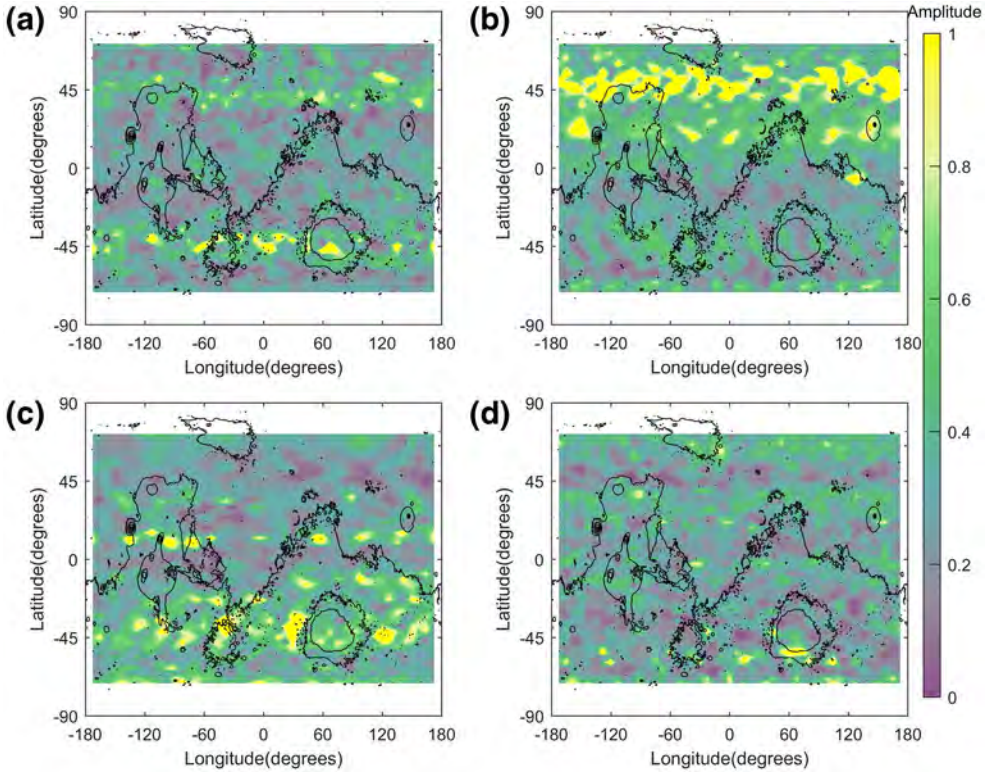

Figure 16. Same plot as Figure 10 but for O hIGWs amplitudes at 240 km. hIGWs, horizontal internal gravity waves.

Acknowledgments
The authors thank NASA Planetary Data System for providing MAVEN ACC and NGIMS data and Luca Montabone for providing the datasets of dust optical depth. The authors would like to thanks Scott England for help on the NGIMS data and the extraction method. The work was supported by the Startup Foundation for Introducing Talent of NUIST, Jiangsu Province Distinguished Professor Project (Grant No. R2018T20) and Key Laboratory of Planetary Sciences Project (Grant No: PSL16_07).

References

Albee, A. L., Palluconi, F., & Arvidson, R. (1998). Mars global surveyor mission: overview and status. *Science*, *279*(5357), 1671–1672. https://doi.org/10.1126/science.279.5357.1671

Bougher, S. W., Cravens, T., Grebowsky, J., & Luhmann, J. (2015). The aeronomy of Mars: Characterization by MAVEN of the upper atmosphere reservoir that regulates volatile escape. *Space Science Reviews*, *195*(1–4), 423–456. https://doi.org/10.1007/s11214-014-0053-7

Bougher, S. W., Jakosky, B., Halekas, J., Grebowsky, J., Luhmann, J., Mahaffy, P., et al. (2015). Early MAVEN Deep Dip campaign reveals thermosphere and ionosphere variability. *Science*, *350*(6261), aad0459. https://doi.org/10.1126/science.aad0459

Bougher, S. W., Roeten, K. J., Olsen, K., Mahaffy, P. R., Benna, M., Elrod, M., et al. (2017). The structure and variability of Mars dayside thermosphere from MAVEN NGIMS and IUVS measurements: Seasonal and solar activity trends in scale heights and temperatures. *Journal of Geophysical Research Space Physics*, *122*(1), 1296–1313. https://doi.org/10.1002/2016JA023454

Cravens, T. E., Rahmati, A., Fox, J. L., Lillis, R., Bougher, S., Luhmann, J., et al. (2017). Hot oxygen escape from Mars: Simple scaling with solar EUV irradiance. *Journal of Geophysical Research: Space Physics*, *122*(1), 1102–1116. https://doi.org/10.1002/2016JA023461

Creasey, J. E., Forbes, J. M., & Keating, G. M. (2006). Density variability at scales typical of gravity waves observed in Mars' thermosphere by the MGS accelerometer. *Geophysical Research Letters*, *33*, L22814. https://doi.org/10.1029/2006GL027583

Deighan, J., Chaffin, M. S., Chaufray, J. Y., Stewart, A. I. F., Schneider, N. M., Jain, S. K., et al. (2015). MAVEN IUVS observation of the hot oxygen corona at Mars. *Geophysical Research Letters*, *42*(21), 9009–9014. https://doi.org/10.1002/2015GL065487

England, S. L., Liu, G., Withers, P., Yiğit, E., Lo, D., Jain, S., et al. (2016a). Simultaneous observations of atmospheric tides from combined in situ and remote observations at Mars from the MAVEN spacecraft. *Journal of Geophysical Research: Planets*, *121*(4), 594–607. https://doi.org/10.1002/2016JE004997

England, S. L., Liu, G., Yiğit, E., Mahaffy, P. R., Elrod, M., Benna, M., et al. (2016b). MAVEN NGIMS Observations of Atmospheric Gravity Waves in the Martian thermosphere. *Journal of Geophysical Research: Space Physics*, *122*, 2310–2335. https://doi.org/10.1002/2016JA023475

Fritts, D. C., Ling, W., Robert, H., & Tolson (2006). Mean and gravity wave structures and variability in the Mars upper atmosphere inferred from Mars Global Surveyor and Mars Odyssey aerobraking densities. *Journal of Geophysical Research: Space Physics*, *111*, A12304. https://doi.org/10.1029/2006JA011897

Jakosky, B. M., Lin, R., Grebowsky, J., Luhmann, J., Mitchell, D., Beutelschies, G., et al. (2015). The Mars Atmosphere and Volatile EvolutioN (MAVEN) mission. *Space Science Reviews*, *195*(1–4), 3–48. https://doi.org/10.1007/s11214-015-0139-x

Jakosky, B. M., Slipski, M., Benna, M., Mahaffy, P., & Alsaeed, N. (2017). Mars' atmospheric history derived from upper-atmosphere measurements of 38 Ar/36 Ar. *Science*, *355*(6332), 1408–1410. https://doi.org/10.1126/science.aai7721

Keating, G., Bougher, S., Zurek, R., Tolson, R., Cancro, G., Noll, S., et al. (1998). The structure of the upper atmosphere of Mars: In situ accelerometer measurements from Mars Global Surveyor. *Science*, *279*(5357), 1672–1676. https://doi.org/10.1126/science.279.5357.1672

Leclercq, L., Williamson, H. N., Johnson, R. E., Tucker, O. J., Tian, L., & Snowden, D. (2020). Molecular kinetic simulations of transient perturbations in a planet's upper atmosphere. *Icarus*, *335*(113394), 1–10. http://dx.doi.org/10.1016/j.icarus.2019.113394

Lefèvre, F., & Krasnopolsky, V. (2017). Atmospheric photochemistry. *The atmosphere and climate of Mars*, *18*, (405–429). Cambridge Planetary Science. https://doi.org/10.1017/9781139060172.013

Liu, J., Jin, S., & Li, Y. (2019). Seasonal Variations and Global Wave Distributions in the Mars Thermosphere From MAVEN and Multisatellites Accelerometer-Derived Mass Densities. *Journal of Geophysical Research: Space Physics*, *124*(11), 9315–9334. https://doi.org/10.1029/2019JA026720

Mahaffy, P. R., Benna, M., King, T., Harpold, D. N., Arvey, R., Barciniak, M., et al. (2015). The neutral gas and ion mass spectrometer on the Mars atmosphere and volatile evolution mission. *Space Science Reviews*, *195*(1–4), 49–73.

McElroy, M. B., & Hunten, D. M. (1970). Photochemistry of CO_2 in the atmosphere of Mars. *Journal of Geophysical Research*, *75*(7), 1188–1201. https://doi.org/10.1029/JA075i007p01188

Medvedev, A. S., & Yiğit, E. (2012). Thermal effects of internal gravity waves in the Martian upper atmosphere. *Geophysical Research Letters*, *39*, L05209. https://doi.org/10.1029/2012GL050852

Medvedev, A. S., & Yiğit, E. (2019). Gravity Waves in Planetary Atmospheres: Their Effects and Parameterization in Global Circulation Models. *Atmosphere*, *10*(9), 531. https://doi.org/10.3390/atmos10090531

Montabone, L., Forget, F., Millour, E., Wilson, R. J., Lewis, S. R., Cantor, B., et al. (2015). Eight-year climatology of dust optical depth on Mars. *Icarus*, *251*, 65–95. https://doi.org/10.1016/j.icarus.2014.12.034

Montabone, L., Spiga, A., Kass, D. M., Kleinböhl, A., Forget, F., & Millour, E. (2020). Martian Year 34 Column Dust Climatology from Mars Climate Sounder Observations: Reconstructed Maps and Model Simulations. *Journal of Geophysical Research: Planets*, *125*(8), http://dx.doi.org/10.1029/2019je006111

Müller-Wodarg, I. C. F., Yelle, R. V., Borggren, N., & Waite, J. H. (2006). Waves and horizontal structures in Titan's thermosphere. *Journal of Geophysical Research*, *111*(A12), A12315. https://doi.org/10.1029/2006JA011961

Rafkin, S. C. R., Sta. Maria, M. R. V., & Michaels, T. I. (2002). Simulation of the atmospheric thermal circulation of a martian volcano using a mesoscale numerical model. *Nature*, *419*(6908), 697–699. https://doi.org/10.1038/nature01114

Siddle, A., Mueller-Wodarg, I., Stone, S., & Yelle, R. (2019). Global characteristics of gravity waves in the upper atmosphere of Mars as measured by MAVEN/NGIMS. *Icarus*, *333*, 12–21. https://doi.org/10.1016/j.icarus.2019.05.021

Smith, M. D. (2009). THEMIS observations of Mars aerosol optical depth from 2002–2008. *Icarus*, *202*(2), 444–452. https://doi.org/10.1016/j.icarus.2009.03.027

Terada, N., Leblanc, F., Nakagawa, H., Medvedev, A. S., Yiğit, E., Kuroda, T., et al. (2017). Global distribution and parameter dependences of gravity wave activity in the Martian upper thermosphere derived from MAVEN/NGIMS observations. *Journal of Geophysical Research: Space Physics*, *122*(2), 2374–2397. https://doi.org/10.1002/2016JA023476

Tolson, R. H., Dwyer, A. M., Hanna, J. L., Keating, G. M., George, B. E., Escalera, P. E., & Werner, M. R. (2005). Application of accelerometer data to Mars Odyssey aerobraking and atmospheric modeling. *Journal of Spacecraft and Rockets*, *42*(3), 435–443. https://doi.org/10.2514/1.15173

Tolson, R. H., Keating, G. M., Zurek, R. W., Bougher, S. W., Justus, C. G., & Fritts, D. C. (2007). Application of accelerometer data to atmospheric modeling during Mars Aerobraking Operations. *Journal of Spacecraft and Rockets*, *44*(6), 1172–1179. https://doi.org/10.2514/1.28472

Vals, M., Spiga, A., Forget, F., Millour, E., & Lott, F. (2019). Study of gravity waves distribution and propagation in the thermosphere of Mars based on MGS, ODY, MRO and MAVEN density measurements. *Planetary and Space Science*, *178*, 104708. https://doi.org/10.1016/j.pss.2019.104708

Wilson, R. J. (2002). Evidence for nonmigrating thermal tides in the Mars upper atmosphere from the Mars Global Surveyor Accelerometer Experiment. *Geophysical Research Letters*, *29*(7), 24–21. https://doi.org/10.1029/2001GL013975

Withers, P. (2006). Mars Global Surveyor and Mars Odyssey Accelerometer observations of the Martian upper atmosphere during aerobraking. *Geophysical Research Letters*, *33*(2), L02201. https://doi.org/10.1029/2005GL024447

Wu, Z., Li, T., Zhang, X., Li, J., & Cui, J. (2020). Dust tides and rapid meridional motions in the Martian atmosphere during major dust storms. *Nature Communications, 11*(1), 1–10. https://doi.org/10.1038/s41467-020-14510-x

Yiğit, E., & Medvedev, A. S. (2010). Internal gravity waves in the thermosphere during low and high solar activity: Simulation study. *Journal of Geophysical Research: Space Physics*, *115*(A8), A00G02,1–16. http://dx.doi.org/10.1029/2009ja015106

Yiğit, E., & Medvedev, A. S. (2015). Internal wave coupling processes in Earth's atmosphere. *Advances in Space Research*, *55*(4), 983–1003. https://doi.org/10.1016/j.asr.2014.11.020

Yiğit, E., Medvedev, A. S., Aylward, A. D., Ridley, A. J., Harris, M. J., Moldwin, M. B., & Hartogh, P. (2012). Dynamical effects of internal gravity waves in the equinoctial thermosphere. *Journal of Atmospheric and Solar-Terrestrial Physics*, *90*, 104–116.

Yiğit, E., Medvedev, A. S., & Hartogh, P. (2015). Gravity waves and high-altitude CO_2 ice cloud formation in the Martian atmosphere. *Geophysical Research Letters*, *42*(11), 4294–4300. https://doi.org/10.1002/2015GL064275

Zurek, R. R. T., Baird, D. M. Z. J., & Bougher, A. S. W. (2015). Application of MAVEN Accelerometer and Attitude Control Data to Mars Atmospheric Characterization. *Space Science Reviews*, *195*(1–4), 303–317. https://doi.org/10.1007/s11214-014-0095-x

Zurek, R. W., & Smrekar, S. E. (2007). An overview of the Mars Reconnaissance Orbiter (MRO) science mission. *Journal of Geophysical Research, 112*(E5), E05S01,1–22. https://doi.org/10.1029/2006je002701

Zurek, R., Tolson, R., Bougher, S., Lugo, R., Baird, D., Bell, J., & Jakosky, B. (2017). Mars thermosphere as seen in MAVEN accelerometer data. *Journal of Geophysical Research: Space Physics*, *122*(3), 3798–3814. https://doi.org/10.1002/2016JA023641